



A General Approach to Convert Hemicyanine Dyes into Highly Optimized Photoacoustic Scaffolds for Analyte Sensing**

Sarah H. Gardner⁺, Catharine J. Brady⁺, Cameron Keeton, Anuj K. Yadav, Sharath C. Mallojjala, Melissa Y. Lucero, Shengzhang Su, Zhengxin Yu, Jennifer S. Hirschi, Liviu M. Mirica, and Jefferson Chan*

Abstract: Most photoacoustic (PA) imaging agents are based on the repurposing of existing fluorescent dye platforms that exhibit non-optimal properties for PA applications. Herein, we introduce PA-HD, a new dye scaffold optimized for PA probe development that features a 4.8-fold increase in sensitivity and a red-shift of the λ_{abs} from 690 nm to 745 nm to enable ratiometric imaging. Computational modeling was used to elucidate the origin of these enhanced properties. To demonstrate the generalizability of our remodeling efforts, we developed three probes for β -galactosidase activity (PA-HD-Gal), nitroreductase activity (PA-HD-NTR), and H_2O_2 (PA-HD- H_2O_2). We generated two cancer models to evaluate PA-HD-Gal and PA-HD-NTR. We employed a murine model of Alzheimer's disease to test PA-HD- H_2O_2 . There, we observed a PA signal increase at 735 nm of 1.79 ± 0.20 -fold relative to background, indicating the presence of oxidative stress. These results were confirmed via ratiometric calibration, which was not possible using the parent HD platform.

Introduction

Photoacoustic imaging is a powerful in vivo approach that is characterized by the generation of ultrasound waves which result from the excitation of an optical absorber with light.^[1] In theory, any light-absorbing material can be induced to afford a photoacoustic readout; however, in practice, only molecules with a wavelength of maximum absorbance in the near-infrared (NIR) region ($\lambda_{\text{abs}} > 650$ nm), a high extinction

coefficient ($\epsilon > 10^4 \text{ M}^{-1} \text{ cm}^{-1}$), and a low quantum yield ($\Phi_{\text{FL}} < 5\%$) are desirable. Initially, when photoacoustic imaging emerged as an in vivo biomedical technique, various endogenous absorbers such as hemoglobin, oxyhemoglobin, and melanin were exploited to provide contrast. These studies set the stage for label-free imaging of various cancer types and inflammatory conditions in human patients.^[2] However, as the demand for improved performance, better contrast, greater target specificity, and molecular information grew, efforts turned toward the design of targeted contrast agents^[3] and activatable photoacoustic probes (also known as acoustogenic probes)^[4] to reliably identify diseased tissue and to monitor biological analytes, respectively.

Owing to the intrinsic similarities between photoacoustic and fluorescence imaging (i.e., the requirement of light excitation), it is reasonable that most photoacoustic imaging agents to date have relied heavily on the repurposing of existing fluorophores. For example, indocyanine green (ICG), an FDA-approved cyanine-based fluorescent dye, was utilized extensively in early studies for contrast-enhanced photoacoustic imaging even though it is prone to photobleaching and oxidative decomposition. Likewise, the first small-molecule activatable photoacoustic probe (designed to detect Cu^{2+})^[5] was based on the aza-BODIPY dye, which is another NIR fluorescent platform.^[6] Subsequent studies have resulted in a palette of aza-BODIPY-based photoacoustic probes for hypoxia,^[7] nitric oxide,^[8] peroxyxynitrite,^[9] hydrogen peroxide,^[10] pH,^[11] redox status,^[12] and photodynamic therapy.^[13] In addition, our group put forth significant efforts to optimize this scaffold for photoacoustic imaging; however, this required the handling of unstable species such as reactive azirine intermediates, as well as challenging (and sometimes low yielding) purifications to separate the desired heteropyrrole coupling product from the unwanted symmetrical aza-BODIPYs.^[14] Due to these limitations, our design has not yet been widely adopted by other probe developers. Beyond aza-BODIPYs, other NIR fluorescent platforms such as xanthenes,^[15] cyanines^[16] and hemicyanine dyes (HD)^[17] have also been repurposed extensively (Scheme 1a).

HDs have attracted considerable attention from the field owing to their ease of synthesis (one-step starting from a parent cyanine and resorcinol) and the presence of a convenient handle (i.e., -OH or -NH₂) to append analyte-responsive triggers.^[18] These features have made HD-based optical probes popular for detecting a diverse range of analytes.^[19] Unfortunately, HDs are far from ideal for photoacoustic analyte sensing. First, the λ_{abs} of a “capped” probe

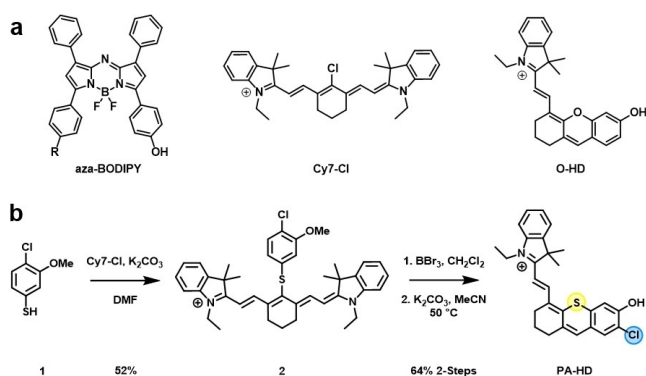
[*] S. H. Gardner,^[+] Prof. J. Chan
Department of Biochemistry
University of Illinois at Urbana-Champaign
Urbana, IL 61801 (USA)
E-mail: jeffchan@illinois.edu

C. J. Brady,^[+] C. Keeton, Dr. A. K. Yadav, M. Y. Lucero, S. Su, Z. Yu,
Prof. L. M. Mirica, Prof. J. Chan
Department of Chemistry and Beckman Institute for Advanced
Science and Technology, University of Illinois at Urbana-Champaign
Urbana, IL 61801 (USA)
Dr. S. C. Mallojjala, Prof. J. S. Hirschi
Department of Chemistry, Binghamton University
Binghamton, NY 13902 (USA)

[+] These authors contributed equally to this work.

[**] A previous version of this manuscript has been deposited on a preprint server (<https://doi.org/10.26434/chemrxiv.14494383.v1>).

Supporting information and the ORCID identification number(s) for the author(s) of this article can be found under:
 <https://doi.org/10.1002/anie.202105905>.



Scheme 1. a) Examples of NIR fluorescent dyes that have been repurposed for photoacoustic applications. b) Synthesis of PA-HD.

(ca. 600) typically falls below the NIR cutoff of 650 nm, as well as the lower wavelength limit of our commercial photoacoustic imaging systems (660 nm (MSOT inVision, iThera) and 680 nm (Nexus 128+, Endra)). These constraints preclude ratiometric calibration which can account for imaging artifacts that result from photobleaching or differential probe clearance. Second, HDs are highly fluorescent molecules ($\Phi_{\text{FL}} \approx 30\text{--}40\%$), meaning less of the excited state will relax via non-radiative decay to afford a photoacoustic signal. In this study, we introduce two highly effective modifications to transform existing HD designs into optimized scaffolds for photoacoustic imaging by substituting the endocyclic oxygen with a sulfur moiety and by tuning the phenolic pK_a value (herein referred to as PA-HDs). To demonstrate generalizability, we prepared three enhanced photoacoustic probes from PA-HD for β -galactosidase activity, nitroreductase activity, and hydrogen peroxide (H_2O_2). The β -galactosidase and nitroreductase probes were evaluated in ovarian and breast cancer models, respectively. Beyond subcutaneous tumors, we also employed our H_2O_2 probe to image oxidative stress in a murine model of Alzheimer's disease.

Results and Discussion

The design of PA-HD is based on the premise that sulfur-substitution can potentially red-shift the λ_{abs} value by up to 50 nm and thus, can facilitate deeper tissue imaging and ratiometric calibration. A similar approach was recently employed to red-shift chemiluminescent probes via sulfur-substitution.^[20] Moreover, we anticipate two additional benefits from this modification that favor photoacoustic imaging. First, we hypothesized the fluorescent quantum yield will be attenuated and second, we expect the extinction coefficient to be enhanced. It is noteworthy that although the apparent pK_a of regular HDs (herein referred to as O-HD) was reported to be ca. 5.6,^[18] this value appears to be inaccurate. In our hands we measured a value of 7.5 (Supporting Information, Figure S1). This discrepancy likely resulted because the pH of each buffer system used to construct the corresponding pH-profile was not adjusted after the organic co-solvent component was added. A high pK_a value will decrease the photo-

acoustic sensitivity and lead to imaging artifacts since the protonated form of O-HD will have a similar absorbance profile to that of the unactivated probe. Therefore, in addition to performing the proposed O to S substitution, it is critical to install an ortho chloro group to lower the phenolic pK_a which ensures that upon unmasking of the trigger, the turned over PA-HD will exist predominantly in a deprotonated form. To this end, we synthesized PA-HD by first substituting the *meso*-chloro group of Cy7-Cl with thiophenol **1** to furnish cyanine **2** in 52% yield. This intermediate was then demethylated with BBr_3 and heated under basic conditions after solvent exchange to initiate the retro-Knoevenagel reaction to generate **PA-HD** in 64% yield over 2-steps (33% overall).

With PA-HD in hand, we first determined that the λ_{abs} was positioned at 745 nm which represents a bathochromic shift of 55 nm relative to O-HD (Figure 1a). Moreover, it is apparent that at pH 7.4, over half the population of O-HD is protonated, and this results in a blue-shifted λ_{abs} and low ϵ . In contrast, since the measured pK_a value of PA-HD is 6.0, over 96% of the dye will be deprotonated at physiological pH (Figure S2). We also found that the ϵ had increased significantly by 62% from $8.2 \times 10^4 \text{ M}^{-1} \text{ cm}^{-1}$ to $13.3 \times 10^4 \text{ M}^{-1} \text{ cm}^{-1}$ and that the Φ_{FL} decreased by six-fold from 30% to 5%. As mentioned previously, meeting these two design criteria will translate into enhanced photoacoustic properties. To evaluate the impact of sulfur-substitution with respect to the photoacoustic signal intensity and potential ratiometric sensing capabilities, we conducted a series of head-to-head in vitro experiments. First, we embedded solutions of each dye (25 μM) in an agar-based tissue phantom (2% milk) and obtained photoacoustic spectra over a wavelength range of 660 to 980 nm (Figure 1b). While the O-HD λ_{abs} clearly fell outside the NIR window, the highest intensity for PA-HD was

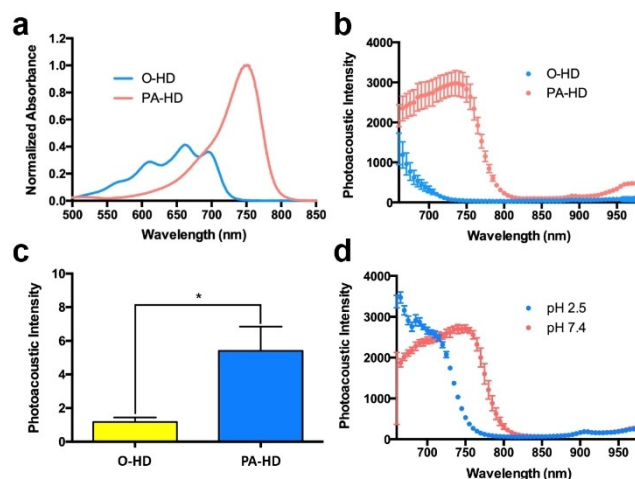


Figure 1. a) Absorbance and b) PA spectra of O-HD and PA-HD at pH 7.4 (1:1 v/v BRB:EtOH). Dye concentration was 25 μM for each dye (Each point represents Mean \pm SD, $n = 3$). c) Normalized photoacoustic intensity of O-HD and PA-HD in a tissue phantom containing 60% milk to mimic scattering effects in dense tissue. [PA-HD] = 0.5 μM (Mean \pm SD, $n = 3$). Statistical analysis was performed using two-tailed Student's t-test ($\alpha = 0.05$), *: $p < 0.05$. d) Photoacoustic spectra of PA-HD at pH 2.5 and 7.4 (Each point represents Mean \pm SD, $n = 3$).

centered at ca. 735 nm. This represents a 4.8-fold increase in sensitivity when comparing the highest signal for each dye. Additionally, we show a dose-dependent increase in the photoacoustic intensity after correcting for wavelength-dependent differences in fluence (Figure S3). Next, we reduced the dye concentration to 0.5 μM and changed the composition of milk in the phantom to 60% to mimic the scattering effects of dense tissue (e.g., brain). Even under these conditions that are designed to attenuate the photoacoustic signal, we could readily detect PA-HD but not O-HD (Figure S4). The corresponding normalized photoacoustic intensities (relative to background) were 5.4 ± 2.5 -fold and 1.18 ± 0.47 -fold, respectively (Figure 1c). To evaluate the potential of this new scaffold for ratiometric imaging, we subjected PA-HD to acidic conditions since protonation of the phenol is an effective proxy for the presence of a trigger at this position. Indeed, the protonated form of PA-HD exhibits a λ_{abs} at 650 nm (Figure S5). The ratios of the deprotonated and protonated forms at 650 nm and 745 nm based on absorbance were found to be 0.36 and 16.81, respectively (Figure 1d). This represents a theoretical turn-on response of 46.7 (defined as $\text{ratio}_{745}/\text{ratio}_{650}$). Similar results were obtained when the experiment was performed at 660 nm (lower wavelength limit) and 735 nm (maximum signal) via photoacoustic imaging to give a turn-on response of 3.7. Together these results demonstrate PA-HD can be employed for ratiometric imaging, while this is not possible with O-HD.

To better understand the origin of these enhanced properties, we modeled O-HD and PA-HD using state-of-the-art computational techniques. The resultant computed spectra at 0 K in acetonitrile shows excellent agreement with the experimental data (Figure S6). Analysis of the computed

geometries (Figure 2a) reveal that the excited states of PA-HD is significantly different from the ground state structures (RMSD 0.2) while the excited state geometry of O-HD remains similar to its ground state (RMSD 0.05). PA-HD is relatively planar in its excited state as evidenced by the dihedral angles involved in the extended π network (ca. 9°). For comparison, the dihedral angle is ca. 20° for the ground state. However, O-HD is planar in both the ground and excited states. Furthermore, the HOMO for the excited state structure of PA-HD exhibits a much higher electron delocalization than the HOMO for the ground state (Figure 2b). We postulate that this increase in planarity for PA-HD, and thereby an increase in the conjugation in the excited state compared to the ground state might be the origin of the better photoacoustic properties observed in PA-HD. Similar behavior is observed in S-HD (an analog lacking the *ortho*-chloro substituent), further supporting our hypothesis (see the Supporting Information for the S-HD results).

Next, we converted PA-HD into a series of three activatable photoacoustic probes to demonstrate that the enhanced properties afforded by the sulfur-substitution are generalizable. Specifically, PA-HD-Gal (Figure 3a), PA-HD-NTR (Figure 3c), and PA-HD- H_2O_2 (Figure 3e) were devel-

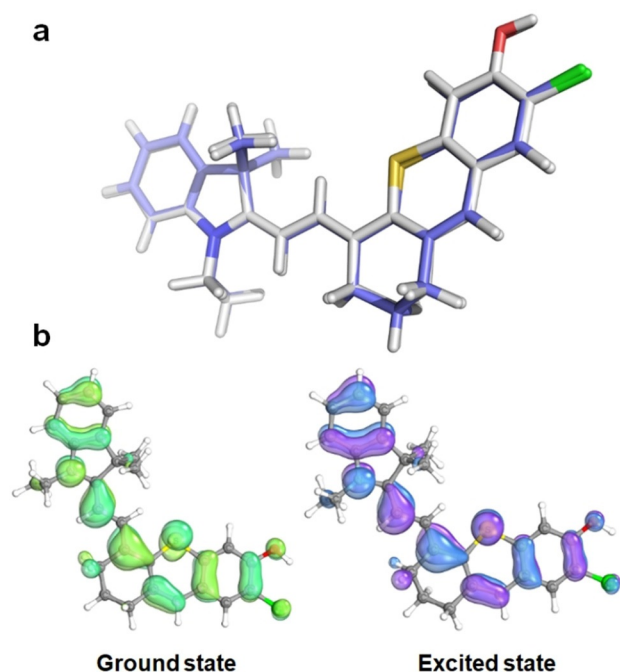


Figure 2. a) An overlay of the excited state geometry (white) with the ground state geometry (blue) for PA-HD. b) The HOMO of the ground state (green) and excited state (blue) structures of PA-HD.

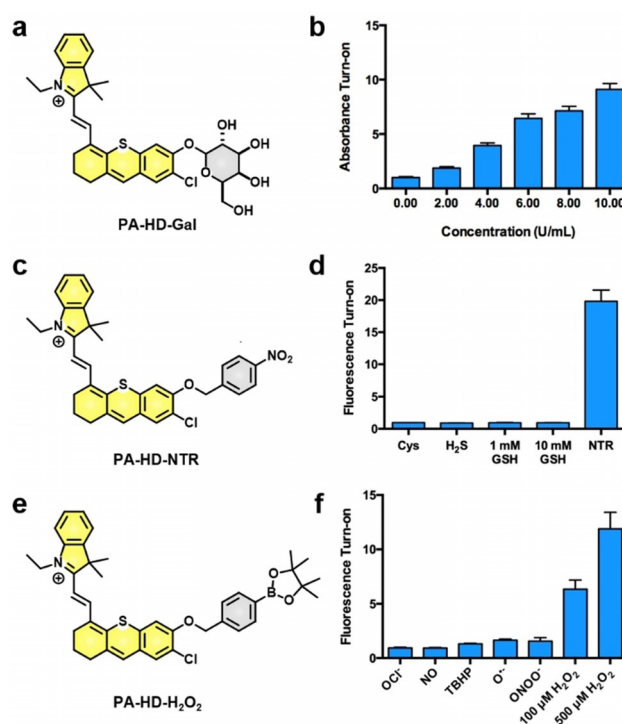


Figure 3. a) Chemical structure of PA-HD-Gal. b) Dose-dependent response of 5 μM PA-HD-Gal after 1 h to 0, 2, 4, 6, 8, or 10 U mL^{-1} of *E. coli* beta-galactosidase at pH 7.4 (9:1 v/v PBS:MeCN) (Mean \pm SD, $n=5$). c) Chemical structure of PA-HD-NTR. d) Response of 2 μM PA-HD-NTR to biologically relevant thiols (Cys and H₂S 100 μM) and GSH at 1 mM and 10 mM for 15 min at pH 7.4 (9:1 v/v PBS:MeCN) (Mean \pm SD, $n=3$). Complete activation mediated by 2 U mL^{-1} *E. coli* nitroreductase. e) Chemical structure of PA-HD-H₂O₂. f) Response of 2 μM PA-HD-H₂O₂ to OCl⁻, NO, TBHP, O₂⁻, ONOO⁻ (100 μM) and H₂O₂ (100 μM and 500 μM) for 1 h at pH 7.4 (9:1 v/v PBS:MeCN) (Mean \pm SD, $n=3$).

oped for β -galactosidase activity, nitroreductase activity, and H_2O_2 , respectively. We selected these three imaging targets because their corresponding triggers are commonly employed to validate new dye systems, and they are important in a host of physiological and pathological processes. For instance, β -galactosidase expression has been used as a marker to identify senescent cells^[21] and ovarian cancer.^[22] Nitroreductase has been used as a target to detect gram positive and negative bacteria,^[23] as well as tumor hypoxia since it is overexpressed in many cancer types under oxygen deficient conditions.^[24] Lastly, H_2O_2 is not only an important signaling molecule, at elevated levels it is a general indicator of oxidative stress in a variety of disease states.^[25]

After synthesizing the three probes, each was subjected to *in vitro* testing to assess target-responsiveness. We found that PA-HD-Gal was readily activated upon incubation with recombinant beta-galactosidase. Specifically, a dose-dependent (0 to 10 $U\text{ mL}^{-1}$) change in the absorbance (shift of the λ_{abs} from 640 to 745 nm) was observed, representing a maximum signal enhancement of 9.1 ± 0.5 -fold based on absorbance (Figure 3b). We confirmed that this increase was due to the enzymatic activity because heat-inactivation of beta-galactosidase prior to incubation with PA-HD-Gal completely attenuated probe activation (Figure S7). Likewise, PA-HD-NTR was activated by recombinant nitroreductase from *E. coli* (19.8 ± 1.7 -fold change in fluorescence after 15 min). Moreover, the probe was demonstrated to be stable in the presence of biological thiols such as Cys, H_2S , and GSH which can potentially reduce the nitro group and lead to 1,4-elimination to give a false response (Figure 3d).^[26] Finally, we determined that PA-HD- H_2O_2 retained its responsiveness to H_2O_2 . In particular, a 6.3 ± 0.8 -fold and 11.9 ± 1.5 -fold change in fluorescence was noted after incubation of the probe for 1 h with 100 μM and 500 μM H_2O_2 , respectively (Figure 3f). In contrast, when PA-HD- H_2O_2 was subjected to selectivity screening against a panel of reactive oxygen/nitrogen species (hypochlorite, nitric oxide, *tert*-butyl hydroperoxide, superoxide, peroxyxynitrite) there was no significant turn-on. Collectively, these results show that installation of established triggers onto PA-HD does not impact their performance. The photophysical properties of all dyes are summarized below in Table 1.

Incubation of PA-HD for 6 h at concentrations up to 10 μM did not significantly impact cell viability (Figure S8). Likewise, the three probes were also not cytotoxic (Figure S9). With these results in hand, we focused our attention

on evaluating the performance of each probe in cell-based studies. Beta-galactosidase is known to be expressed in ovarian cancer presumably because it is involved in the processing of glycans such as sialyl Lewis x.^[27] Upon incubation of two human ovarian cancer cell lines, OVCAR-3 and IGROV-1, with PA-HD-Gal, we were able to observe a cytosolic staining pattern which suggests our probe was being activated by beta-galactosidase (Figure 4a). To confirm these results, we synthesized BGA, a potent beta-galactosidase inhibitor,^[28] to determine whether pretreatment would attenuate probe activation. Relative to OVCAR-3 and IGROV-1 cells that were not treated with the inhibitor, the signal intensity was 2.18-fold and 2.78-fold lower, respectively (Figure 4b). Next, the ability of PA-HD-NTR to distinguish between normoxic and hypoxic conditions via nitroreductase activity was tested. ID8 cancer cells were cultured in 20%, 5%, 2%, or 1% oxygen atmospheres for ca. 6 h before treatment with PA-HD-NTR. Under oxygen deficient conditions, nitroreductases present within cells can convert the aryl nitro group to the corresponding hydroxyl amine or amino moieties via multiple single electron transfer events. This reduction can facilitate unmasking of PA-HD via self-immolative chemistry. As anticipated, the signal was barely discernable from background when PA-HD-NTR was incubated under normoxic conditions (20% O_2) (Figure 4c). In contrast, the intensity was 1.38 ± 0.10 -fold higher at 1% oxygen (Figure 4d). Importantly, the low signal enhancement is a consequence of the trigger which requires chronic hypoxic conditions to upregulate nitroreductase expression. Finally, NeuroScreen-1 cells, a model system for neurons, was stained with PA-HD- H_2O_2 and treated with 0, 25, 50, or 100 μM H_2O_2 (Figure 4e). We selected this cell line because oxidative stress plays a central role in neurodegenerative diseases, as well as aging of the brain. Our results revealed a dose-dependent increase in the signal intensity where the highest concentration of H_2O_2 resulted in a 19.3 ± 7.4 -fold turn-on response after incubation (Figure 4f).

Next, we generated syngeneic models of ovarian cancer and breast cancer using ID8 and 4T1 cells, respectively. Intratumoral injections were employed to administer PA-HD-Gal to the ovarian tumors and PA-HD-NTR to the breast tumors. We selected this route of administration, as opposed to systemic injection, because we wanted to directly compare the signal change with the non-tumor bearing flank which can be treated with the same amount of probe via subcutaneous injection. Typically, we utilize tumors with a volume of at least

200–500 mm^3 for imaging purposes; however, to test PA-HD-Gal, the average volume was only ca. 30 mm^3 to showcase the enhanced sensitivity afforded by PA-HD. After 2.5 h, cross-sectional photoacoustic images were acquired at 735 nm using a MSOT imaging system to detect the turned over product. We observed a turn-on response (defined as the photoacoustic signal at 2.5 h over the initial scan) of 1.31 ± 0.21 -fold in

Table 1: Summary of photophysical properties.

Compound	$\lambda_{\text{abs}}^{[a]}$ [nm]	$\lambda_{\text{em}}^{[a]}$ [nm]	$\epsilon^{[a]}$ [$\times 10^4\text{ M}^{-1}\text{ cm}^{-1}$]	$\phi_f^{[a,b]}$ [%]	PABF [$\times 10^4$]	$pK_a^{[c]}$
O-HD	690	712	8.2	30	5.7	7.5
PA-HD	745	765	13.3	5	12.6	6.0
PA-HD-Gal	640	728	3.8	0.7	3.8	N.D.
PA-HD-NTR	642	735	2.7	0.7	2.8	N.D.
PA-HD- H_2O_2	645	738	2.8	0.7	2.7	N.D.

[a] Determined at pH 8.25 in 1:1 v/v PBS:MeOH. [b] vs. ICG in DMSO. [c] pK_a values determined in 1:1 v/v Britton–Robinson buffers ranging from pH 2.6 to 11.3. N.D. = Not determinable.

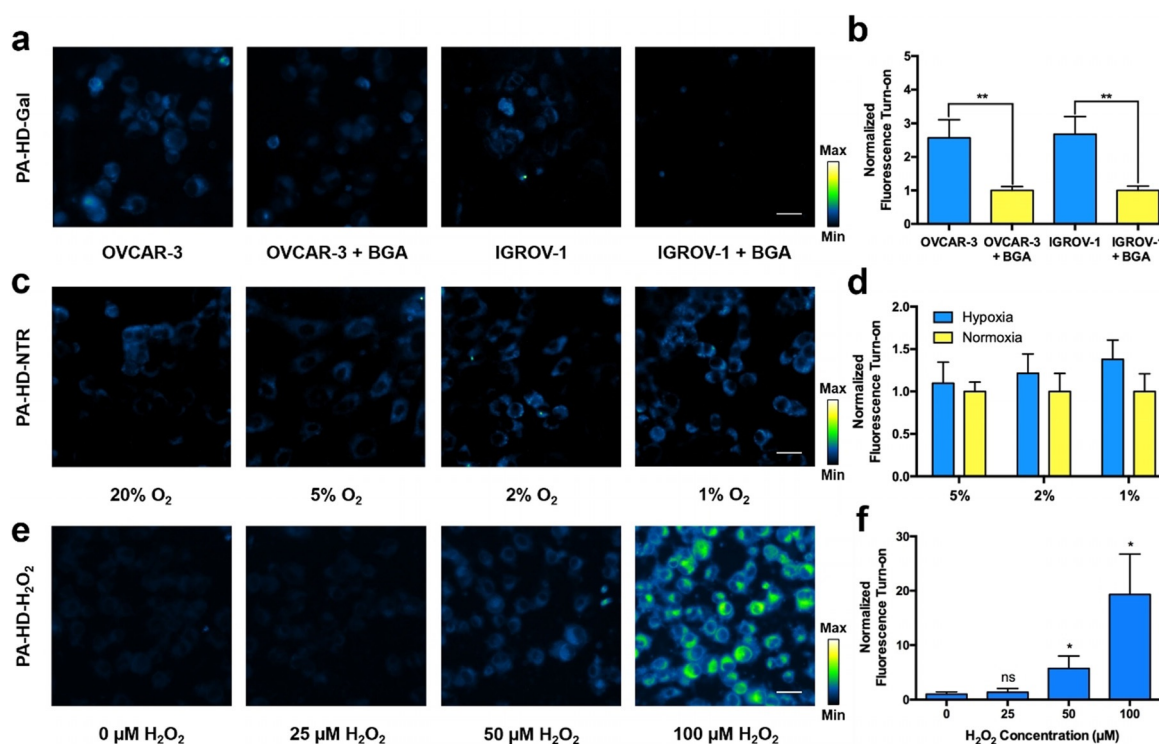


Figure 4. a) Fluorescent images of PA-HD-Gal (4 μM) in ovarian cancer cell lines (OVCAR-3 and IGROV-1) pre-treated with a vehicle control or BGA, a beta-galactosidase inhibitor (1.5 mM). $n=3$ for each condition. b) Quantified data from (a) normalized to inhibitor condition (Mean \pm SD, $n=3$). Statistical analysis was performed using two-tailed Student's *t*-test ($\alpha=0.05$), **: $p < 0.01$. c) Fluorescent images of PA-HD-NTR (2 μM) in ID8 cells cultured under the indicated oxygen atmosphere (20, 5, 2, or 1% oxygen). $n=3$ for each condition. d) Quantified data from (c) normalized to a normoxic control (Mean \pm SD, $n=3$). e) Fluorescent Images of PA-HD-H₂O₂ (10 μM) in NeuroScreen-1 cells treated with various concentrations of H₂O₂ (0, 25, 50 100 μM). $n=3$ for each condition. f) Quantified data from (e) normalized to the 0 μM H₂O₂ condition (Mean \pm SD, $n=3$). Statistical analysis was performed using two-tailed Student's *t*-test ($\alpha=0.05$) compared to 0 μM condition, *: $p < 0.05$. Scale bar represents 50 μm.

the tumor. In contrast, there was no change (0.99 ± 0.10) for the PA-HD-Gal-treated flanks (Figure S10). These results were confirmed via *ex vivo* photoacoustic imaging because photoacoustic-active dark skin patches appeared directly over the tumor site as a consequence of shaving and use of depilatory cream to prepare the C57BL/6 mice for ID8 cell implantation (a common occurrence with this strain). We obtained similar results when PA-HD-NTR was utilized to detect hypoxia in 4T1 tumors. 1.5 h after administration of the probe, the signal intensity at 735 nm increased by 1.40 ± 0.24 -fold relative to the non-tumor flank which changed by 1.09 ± 0.10 -fold (Figure S11). As mentioned previously, in our hands, the nitroreductase trigger only yields a modest change since there is a requirement on the overexpression of nitroreductase.

Finally, beyond subcutaneous tumor models, it is critical for us to evaluate whether the enhanced photoacoustic properties of PA-HD will effectively translate in a deep-tissue context. We sought to employ PA-HD-H₂O₂ to image oxidative stress (via H₂O₂ detection) in an Alzheimer's disease model. The brain consumes massive amounts of oxygen to fuel its stringent metabolic demands.^[29] However, when the natural antioxidant defense systems of the brain are compromised, a net increase in the generation of reactive

oxygen species will result. Since oxidative stress is a hallmark of many neurological disorders including Alzheimer's disease,^[30] it is reasonable to assume that H₂O₂ will be elevated in the brain; however, there is limited direct evidence showing this to be true at the molecular level.^[31] In our study, we systemically administered PA-HD-H₂O₂ to 5xFAD mice which is a well-established transgenic model engineered to express the human amyloid beta protein precursor.^[32] We employed photoacoustic imaging at 660 nm to track probe uptake and observed a signal increase at this wavelength that plateaued after ca. 1 h. Of note, uptake of similar positively charged dyes through the blood-brain barrier have been reported in murine models of Alzheimer's disease.^[33] To ensure sufficient time for probe activation, we waited a total of 2.5 h before irradiating the brain at 735 nm (Figure 5a). A marked increase in the photoacoustic signal at this wavelength relative to the initial timepoint was observed (1.79 ± 0.20 -fold increase) indicating conversion of PA-HD-H₂O₂ to PA-HD (Figure 5b). In contrast, the turn-on response for healthy wildtype controls (B6SJL/F1/J mice) was only 1.02 ± 0.14 -fold. To corroborate these results, we turned to ratio-metric analysis (Figure 5b). We hypothesized the PA₇₃₅/PA₆₆₀ ratio will be higher in the 5xFAD mice compared to the B6SJL/F1/J mice at the 2.5 h timepoint since this would

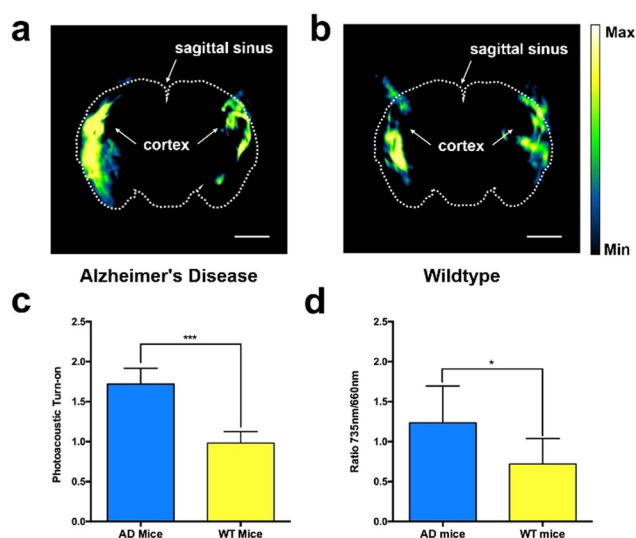


Figure 5. Representative photoacoustic images of the brain from a) an Alzheimer's disease mouse and b) a wildtype mouse captured 2.5 h after PA-HD-H₂O₂ was administered via retroorbital injection with excitation provided at 735 nm. Scale bar represents 2.5 mm. Dotted white outline of the brain is for visualization purposes only. Brain region cropped and overlaid onto a dark background. c) Photoacoustic turn-on response for Alzheimer's disease mice ($n=5$) and wildtype mice ($n=6$). Error bars = SD. Statistical analysis was performed using two-tailed Student's t-test ($\alpha=0.05$), ***: $p < 0.001$. d) Photoacoustic ratio at 735 nm/660 nm of data from (c) (Error bars = SD). Statistical analysis was performed using the Mann-Whitney U test ($\alpha=0.05$), *: $p < 0.05$.

represent probe activation and generation of PA-HD. Indeed, the ratio for the 5xFAD mice was 1.23 ± 0.46 , whereas the ratio for the B6SJLF1/J mice was 0.85 ± 0.07 . It is important to emphasize that ratiometric imaging would not have been possible with O-HD.

Conclusion

At the onset of this study, our goal was to establish a new dye platform that is optimized for the development of activatable photoacoustic probes. This approach represents a significant departure from the common practice of repurposing NIR fluorescent dyes that exhibit sub-optimal properties for photoacoustic imaging. One of the key criteria that we prioritized when developing PA-HD was accessibility, since we believe a high synthetic overhead (about eight steps) would be less desirable to probe developers in the field. The O-HD dye developed by Lin and co-workers represents an attractive starting point for our remodeling efforts because it can be prepared from Cy7-Cl and resorcinol in a single step and has been shown to be a versatile platform for various biological applications. Beginning from 4-chloro-3-methoxybenzenethiol, PA-HD can be prepared in only three-steps with an overall yield of 33.3%. In this study, we demonstrated that substitution of the endocyclic oxygen atom with a sulfur group affords many desired properties. For instance, we observed a red-shifted λ_{abs} of 55 nm which facilitated access to

deeper tissue and enabled ratiometric imaging. The ability to confirm an in vivo imaging result by tracking the signal change at two wavelengths clearly sets PA-HD apart from O-HD. While spectral unmixing is another strategy we could have potentially utilized to isolate the signal of PA-HD-H₂O₂ from that of background, this requires us to obtain a high-quality in vivo spectrum of the probe which we were unable to do in this instance. This highlights why ratiometric imaging is so critical. It is noteworthy that while we were evaluating the photoacoustic properties of PA-HD, a group prepared a NIR fluorescent probe based on a similar platform (lacking the *ortho*-chloro group and a different *N*-alkylation pattern) to image cysteine in live cells.^[34] However, as we have demonstrated in this work, sulfur-substitution results in a significant decrease in the fluorescent quantum yield which favors photoacoustic imaging while rendering the dye less effective for optical imaging. Indeed, to acquire the fluorescent cell images featured in Figure 3, it was necessary for us to irradiate with the light source set at 100% power in some instances. With this in mind, we envision PA-HD will facilitate the development of a diverse range of new activatable photoacoustic probes. We are optimistic that this work will result in a divergence between O-HD-based probes for fluorescent applications and PA-HD-based chemical tools for photoacoustic imaging.

Acknowledgements

The authors acknowledge the National Institutes of Health for support (R35GM133581 to J.C.; R01GM114588 to L.M.M.; R15GM142103-01 to J.S.H.). S.C.M. acknowledges the supercomputing resources provided by XSEDE grant (TG-CHE200009). C.J.B. acknowledges the Chemistry-Biology Interface Training Grant (T32-GM136629) and Robert C. and Carolyn J. Springborn Graduate Fellowship for support. M.Y.L. thanks the Alfred P. Sloan Foundation for financial support. Major funding for the 500 MHz Bruker CryoProbe was provided by the Roy J. Carver Charitable Trust (Muscatine, Iowa; Grant No. 15-4521) to the School of Chemical Sciences NMR Lab. The Q-ToF Ultima mass spectrometer was purchased in part with a grant from the National Science Foundation, Division of Biological Infrastructure (DBI-0100085). We also acknowledge Dr. Iwona Dobrucka and the Molecular Imaging Laboratory at the Beckman Institute for use of the IVIS imaging system, Prof. Erik R. Nelson (Molecular and Integrative Physiology, UIUC) for ID8 and IGROV-1 cells, Prof. Kai Zhang (Biochemistry, UIUC) for NeuroScreen-1 cells, Sandy McMasters (UIUC Cell Media Facility) for help with preparation of cell culture media and technical expertise and Dr. Andrew Brannen (iThera Medical) for helpful suggestions.

Conflict of Interest

The authors declare no conflict of interest.

Keywords: acoustogenic probe · Alzheimer's disease · analyte sensing · hydrogen peroxide · photoacoustic imaging

- [1] a) L. V. Wang, S. Hu, *Science* **2012**, *335*, 1458; b) A. K. Yadav, S. Hernandez, S. Su, J. Chan, *Curr. Opin. Chem. Biol.* **2020**, *57*, 114–121.
- [2] I. Steinberg, D. M. Huland, O. Vermesh, H. E. Frostig, W. S. Tummers, S. S. Gambhir, *Photoacoustics* **2019**, *14*, 77–98.
- [3] J. Weber, P. C. Beard, S. E. Bohndiek, *Nat. Methods* **2016**, *13*, 639–650.
- [4] a) C. J. Reinhardt, J. Chan, *Biochemistry* **2018**, *57*, 194–199; b) H. J. Knox, J. Chan, *Acc. Chem. Res.* **2018**, *51*, 2897–2905.
- [5] H. Li, P. Zhang, L. P. Smaga, R. A. Hoffman, J. Chan, *J. Am. Chem. Soc.* **2015**, *137*, 15628–15631.
- [6] Y. Ge, D. F. O'Shea, *Chem. Soc. Rev.* **2016**, *45*, 3846–3864.
- [7] a) H. J. Knox, J. Hedhli, T. W. Kim, K. Khalili, L. W. Dobrucki, J. Chan, *Nat. Commun.* **2017**, *8*, 1794; b) H. J. Knox, T. W. Kim, Z. Zhu, J. Chan, *ACS Chem. Biol.* **2018**, *13*, 1838–1843; c) M. Chen, H. J. Knox, Y. Tang, W. Liu, L. Nie, J. Chan, J. Yao, *Opt. Lett.* **2019**, *44*, 3773–3776.
- [8] a) C. J. Reinhardt, E. Y. Zhou, M. D. Jorgensen, G. Partipilo, J. Chan, *J. Am. Chem. Soc.* **2018**, *140*, 1011–1018; b) E. Y. Zhou, H. J. Knox, C. J. Reinhardt, G. Partipilo, M. J. Nilges, J. Chan, *J. Am. Chem. Soc.* **2018**, *140*, 11686–11697; c) C. J. Reinhardt, R. Xu, J. Chan, *Chem. Sci.* **2020**, *11*, 1587–1592.
- [9] J. Zhang, X. Zhen, P. K. Upputuri, M. Pramanik, P. Chen, K. Pu, *Adv. Mater.* **2017**, *29*, 1604764.
- [10] X. Lu, M. Zhao, P. Chen, Q. Fan, W. Wang, W. Huang, *J. Mater. Chem. B* **2018**, *6*, 4531–4538.
- [11] J. Geng, W. Li, L. P. Smaga, N. R. Sottos, J. Chan, *Chem. Mater.* **2018**, *30*, 2198–2202.
- [12] J. Zheng, Q. Zeng, R. Zhang, D. Xing, T. Zhang, *J. Am. Chem. Soc.* **2019**, *141*, 19226–19230.
- [13] a) Q. Tang, W. Si, C. Huang, K. Ding, W. Huang, P. Chen, Q. Zhang, X. Dong, *J. Mater. Chem. B* **2017**, *5*, 1566–1573; b) Y. Gawale, N. Adarsh, S. K. Kalva, J. Joseph, M. Pramanik, D. Ramaiah, N. Sekar, *Chem. Eur. J.* **2017**, *23*, 6570–6578.
- [14] E. Y. Zhou, H. J. Knox, C. Liu, W. Zhao, J. Chan, *J. Am. Chem. Soc.* **2019**, *141*, 17601–17609.
- [15] a) S. Wang, G. Yu, Y. Ma, Z. Yang, Y. Liu, J. Wang, X. Chen, *ACS Appl. Mater. Interfaces* **2019**, *11*, 1917–1923; b) Y. Mantri, B. Davidi, J. E. Lemaster, A. Hariri, J. V. Jokerst, *Nanoscale* **2020**, *12*, 10511–10520; c) H.-W. Liu, H. Zhang, X. Lou, L. Teng, J. Yuan, L. Yuan, X.-B. Zhang, W. Tan, *Chem. Commun.* **2020**, *56*, 8103–8106; d) T. Ikeno, K. Hanaoka, S. Iwaki, T. Myochin, Y. Murayama, H. Ohde, T. Komatsu, T. Ueno, T. Nagano, Y. Urano, *Anal. Chem.* **2019**, *91*, 9086–9092; e) F. Liu, X. Shi, X. Liu, F. Wang, H.-B. Yi, J.-H. Jiang, *Chem. Sci.* **2019**, *10*, 9257–9264.
- [16] a) A. Mishra, Y. Jiang, S. Roberts, V. Ntziachristos, G. G. Westmeyer, *Anal. Chem.* **2016**, *88*, 10785–10789; b) J. Zhang, L. P. Smaga, N. S. R. Satyavolu, J. Chan, Y. Lu, *J. Am. Chem. Soc.* **2017**, *139*, 17225–17228; c) S. Roberts, M. Seeger, Y. Jiang, A. Mishra, F. Sigmund, A. Stelzl, A. Lauri, P. Symvoulidis, H. Rolbieski, M. Preller, X. L. Deán-Ben, D. Razansky, T. Orschmann, S. C. Desbordes, P. Vetschera, T. Bach, V. Ntziachristos, G. G. Westmeyer, *J. Am. Chem. Soc.* **2018**, *140*, 2718–2721; d) H. Xiao, C. Wu, P. Li, W. Gao, W. Zhang, W. Zhang, L. Tong, B. Tang, *Chem. Sci.* **2017**, *8*, 7025–7030; e) Y. Liu, S. Wang, Y. Ma, J. Lin, H.-Y. Wang, Y. Gu, X. Chen, P. Huang, *Adv. Mater.* **2017**, *29*, 1606129; f) G. Ma, X. Gao, C. Jiang, S. Xing, C. Wei, P. Huang, J. Lin, *Anal. Chem.* **2019**, *91*, 13570–13575; g) Y. Zhang, S. He, W. Chen, Y. Liu, X. Zhang, Q. Miao, K. Pu, *Angew. Chem. Int. Ed.* **2021**, *60*, 5921–5927; *Angew. Chem.* **2021**, *133*, 5986–5992; h) X. Meng, J. Zhang, Z. Sun, L. Zhou, G. Deng, S. Li, W. Li, P. Gong, L. Cai, *Theranostics* **2018**, *8*, 6025–6034; i) C. Zhang, R. Gao, L. Zhang, C. Liu, Z. Yang, S. Zhao, *Anal. Chem.* **2020**, *92*, 6382–6390; j) M. Y. Lucero, A. K. East, C. J. Reinhardt, A. C. Sedgwick, S. Su, M. C. Lee, J. Chan, *J. Am. Chem. Soc.* **2021**, *143*, 7196; k) X. Li, Y. Tang, J. Li, X. Hu, C. Yin, Z. Yang, Q. Wang, Z. Wu, X. Lu, W. Wang, W. Huang, Q. Fan, *Chem. Commun.* **2019**, *55*, 5934–5937.
- [17] a) Y. Wu, S. Huang, J. Wang, L. Sun, F. Zeng, S. Wu, *Nat. Commun.* **2018**, *9*, 3983; b) L. Sun, Y. Wu, J. Chen, J. Zhong, F. Zeng, S. Wu, *Theranostics* **2019**, *9*, 77–89; c) T. Ma, J. Zheng, T. Zhang, D. Xing, *Nanoscale* **2018**, *10*, 13462–13470; d) P. Cheng, W. Chen, S. Li, S. He, Q. Miao, K. Pu, *Adv. Mater.* **2020**, *32*, 1908530; e) W. Gao, X. Li, Z. Liu, W. Fu, Y. Sun, W. Cao, L. Tong, B. Tang, *Anal. Chem.* **2019**, *91*, 1150–1156; f) Q. Zeng, Y. Wu, T. Zhang, *J. Innovative Opt. Health Sci.* **2019**, *12*, 1941001; g) X. Gao, G. Ma, C. Jiang, L. Zeng, S. Jiang, P. Huang, J. Lin, *Anal. Chem.* **2019**, *91*, 7112–7117; h) J. Huang, Y. Wu, F. Zeng, S. Wu, *Theranostics* **2019**, *9*, 7313–7324; i) M. Y. Lucero, J. Chan, *Towards Personalized Medicine: Photoacoustic Imaging Enables Companion Diagnosis and Targeted Treatment of Lung Cancer*, **2020**, <https://doi.org/10.26434/chemrxiv.11888214.v2>.
- [18] L. Yuan, W. Lin, S. Zhao, W. Gao, B. Chen, L. He, S. Zhu, *J. Am. Chem. Soc.* **2012**, *134*, 13510–13523.
- [19] a) J. Huang, J. Li, Y. Lyu, Q. Miao, K. Pu, *Nat. Mater.* **2019**, *18*, 1133–1143; b) S. He, J. Li, Y. Lyu, J. Huang, K. Pu, *J. Am. Chem. Soc.* **2020**, *142*, 7075–7082; c) Y. Yang, T. Zhou, M. Jin, K. Zhou, D. Liu, X. Li, F. Huo, W. Li, C. Yin, *J. Am. Chem. Soc.* **2020**, *142*, 1614–1620.
- [20] J. Huang, Y. Jiang, J. Li, J. Huang, K. Pu, *Angew. Chem. Int. Ed.* **2021**, *60*, 3999–4003; *Angew. Chem.* **2021**, *133*, 4045–4049.
- [21] F. Debacq-Chainiaux, J. D. Erusalimsky, J. Campisi, O. Toussein, *Nat. Protoc.* **2009**, *4*, 1798–1806.
- [22] D. Asanuma, M. Sakabe, M. Kamiya, K. Yamamoto, J. Hiratake, M. Ogawa, N. Kosaka, P. L. Choyke, T. Nagano, H. Kobayashi, Y. Urano, *Nat. Commun.* **2015**, *6*, 6463.
- [23] R. H. F. Wong, T. Kwong, K.-H. Yau, H. Y. Au-Yeung, *Chem. Commun.* **2015**, *51*, 4440–4442.
- [24] W. Qin, C. Xu, Y. Zhao, C. Yu, S. Shen, L. Lin, W. Huang, *Chin. Chem. Lett.* **2018**, *29*, 1451–1455.
- [25] H. Iwashita, E. Castillo, M. S. Messina, R. A. Swanson, C. J. Chang, *Proc. Natl. Acad. Sci. USA* **2021**, *118*, e2018513118.
- [26] L. A. Montoya, M. D. Pluth, *Chem. Commun.* **2012**, *48*, 4767–4769.
- [27] R. Saldova, L. Royle, C. M. Radcliffe, U. M. Abd Hamid, R. Evans, J. N. Arnold, R. E. Banks, R. Hutson, D. J. Harvey, R. Antrobus, S. M. Petrescu, R. A. Dwek, P. M. Rudd, *Glycobiology* **2007**, *17*, 1344–1356.
- [28] W. Guo, J. Hiratake, K. Ogawa, M. Yamamoto, S. J. Ma, K. Sakata, *Bioorg. Med. Chem. Lett.* **2001**, *11*, 467–470.
- [29] M. E. Watts, R. Pocock, C. Claudianos, *Front. Mol. Neurosci.* **2018**, *11*, 00216.
- [30] W.-J. Huang, X. Zhang, W.-W. Chen, *Biomed. Rep.* **2016**, *4*, 519–522.
- [31] a) J. Yang, J. Yang, S. H. Liang, Y. Xu, A. Moore, C. Ran, *Sci. Rep.* **2016**, *6*, 35613; b) J. Yang, X. Zhang, P. Yuan, J. Yang, Y. Xu, J. Grutzendler, Y. Shao, A. Moore, C. Ran, *Proc. Natl. Acad. Sci. USA* **2017**, *114*, 12384.
- [32] M. B. Dinkins, S. Dasgupta, G. Wang, G. Zhu, Q. He, J. N. Kong, E. Bieberich, *J. Alzheimer's Dis.* **2015**, *46*, 55–61.
- [33] a) S.-J. Park, C. J. H. Ho, S. Arai, A. Samanta, M. Olivo, Y.-T. Chang, *Sci. Rep.* **2019**, *9*, 12052; b) M. D. Sweeney, A. P. Sagare, B. V. Zlokovic, *Nat. Rev. Neurol.* **2018**, *14*, 133–150.
- [34] S. Cai, C. Liu, X. Jiao, L. Zhao, X. Zeng, *J. Mater. Chem. B* **2020**, *8*, 2269–2274.

Manuscript received: April 30, 2021

Revised manuscript received: May 26, 2021

Accepted manuscript online: June 5, 2021

Version of record online: July 1, 2021